

---

# Controlled Dynamics Attractor Transformer

---

Cheng Zhang<sup>1</sup> Minnan Luo<sup>1</sup> Zesheng Yang<sup>1</sup> Ming Li<sup>2</sup> Yong-Jin Liu<sup>2</sup> Qinghua Zheng<sup>1</sup>

## Abstract

Transformer architectures have dramatically advanced representation learning and inference in deep models through self-attention mechanisms. In parallel, associative memory frameworks map representations onto energy landscapes, offering interpretable retrieval mechanisms. However, their continuous-time inference dynamics lack the biological plausibility of classical Continuous Attractor Neural Networks. To bridge this gap, we propose **Controlled Dynamics Attractor Transformer (CDAT)**, which couples a mixture von Mises–Fisher attention energy with a Hopfield refinement energy, while augmenting energy descent with a CANN-inspired excitation–inhibition modulation. CDAT instantiates a topology-constrained dynamical system whose couplings encode relational structure among tokens, thereby linking attractor-style dynamics to modern energy-based attention. We further provide a constructive dissipation analysis to formally establish their controlled inference dynamics. Benefiting from these robust and structured dynamics, CDAT achieves state-of-the-art performance across multiple benchmarks in graph anomaly detection and graph classification.

## 1. Introduction

Transformer-style attention has emerged as the cornerstone of information routing in modern deep networks. However, in realistic scenarios characterized by noisy observations, adversarial perturbations, and complex relational dependencies, the update dynamics of token representations often prove fragile. Small deviations can propagate and amplify through repeated interactions, causing trajectories to drift to-

ward spurious states, and global mixing can wash out locally meaningful structure (Davis et al., 2021). This motivates a question that is largely orthogonal to block-level heuristics: can we explicitly endow attention-driven representation updates with a notion of stability and attraction, ensuring that iterative inference converges reliably to meaningful states rather than merely producing a feed-forward output?

A natural solution emerges from attractor dynamics in cognitive science and neural computation. Associative (semantic) memory explains how biological systems robustly recover latent content from partial cues (Krotov & Hopfield, 2016; 2021)—a behavior computationally modeled as content-addressable memory. In this process, complete patterns are reconstructed from degraded queries by evolving neural activity toward stable states (Hinton & Anderson, 2014; Rolls, 2013; Tsodyks & Sejnowski, 1995). This perspective suggests modeling representation learning as an iterative state evolution that relaxes toward stable attractors shaped by a global objective.

Modern advancements in Associative Memory (AM) model make this connection concrete. Hopfield networks and their dense/continuous variants provide recurrent dynamics governed by an explicit energy function, and recent results reveal softmax attention as a special case of these models (Ramsauer et al., 2021; Bricken & Pehlevan, 2021). From this perspective, stability is intrinsic rather than incidental: the existence of a global energy landscape imposes rigorous constraints on permissible operations and parameter symmetries, theoretically guaranteeing the convergence of the forward computation (Saha et al., 2023).

In addition, Energy Transformer (ET) operationalizes this principle by starting from a task-tailored energy function and deriving an iterative Transformer-like block as a consequence of minimizing that energy (Hoover et al., 2023). Instead of stacking many conventional blocks, ET iterates token representations within a single energy-based block until (approximate) convergence, turning inference into an interpretable dynamical system that can be inspected through update directions over time.

A key motivation for our design arises from the limitations of discrete attractor models. Classic Hopfield-type networks excel at robust retrieval over finite pattern sets (Amit et al., 1985; Amit, 1989), yet their basins typically collapse mem-

<sup>1</sup>School of Computer Science and Technology, MOEK-LINNS Lab, Xi’an Jiaotong University, Xi’an, Shaanxi, China  
<sup>2</sup>Department of Computer Science and Technology, Tsinghua University, Beijing, China. Correspondence to: Minnan Luo <minnluo@xjtu.edu.cn>.

ories into isolated point attractors, which becomes restrictive when latent factors vary continuously. Continuous Attractor Neural Networks (CANNs) offer a complementary perspective: under approximately symmetric interactions, they sustain stable activity profiles that drift smoothly along low-dimensional manifolds (Amari, 1977; Samsonovich & McNaughton, 1997; Mi et al., 2014). In structured settings, however, relational interactions (*e.g.*, graph topology) are typically heterogeneous (Hamilton et al., 2017), rendering the manifold view only approximate. Practically, the dynamics still converge to discrete stable states by absorbing relational information, producing basins that better align with the data geometry and thus improving robustness and retrieval quality.

Accordingly, we inject CANN-inspired mechanisms into modern Hopfield-type associative memory via a continuous-attractor-inspired modulation that implements local excitation and global inhibition under structurally modulated feedback. The goal is not to enforce a literal continuous attractor manifold, but to reshape the energy landscape and its induced trajectories so that the resulting discrete attractors become topology-aware and less prone to spurious convergence. More broadly, this modulation introduces a new control interface over attractor dynamics: instead of treating inference as a purely monotone descent along the energy negative gradient (Hoover et al., 2023), we expose additional, principled degrees of freedom for steering, damping, and stabilizing the state evolution. This challenges the conventional view that associative memory dynamics need only be driven by energy descent (Hopfield, 1982; Ramsauer et al., 2021), and positions our framework as a more expressive and controllable platform for iterative inference.

In this paper, we propose the Controlled Dynamics Attractor Transformer (CDAT), an energy-based Transformer framework with a clearer division of computational roles and a more controllable attractor geometry. CDAT integrates two complementary energy components—for coarse directional alignment and fine-grained prototype retrieval—with a CANN-inspired modulation mechanism (Hamilton et al., 2017; Wu et al., 2021). This design explicitly stabilizes the attractor geometry against spurious states while preserving structural fidelity. As illustrated in Fig. 1, this mechanism enables CDAT to escape spurious local minima that entrap standard energy descent schemes. Specifically, our main contributions are threefold:

- We propose CDAT, an energy-based Transformer framework that develops a structure-aware modulation mechanism inspired by CANNs. By coupling this with explicit stabilization, we achieve controllable attractor dynamics beyond naive energy descent. The resulting topology-induced attractors suppress spurious states and oscillations, improving robustness on

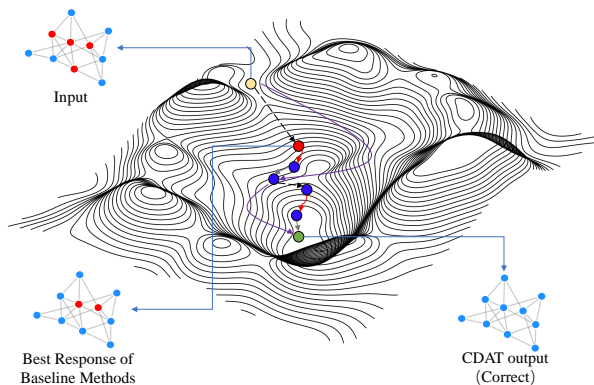


Figure 1. CDAT dynamics. The figure shows the representation trajectories on the energy landscape. While the negative-gradient baseline (black dashed) gets trapped in a spurious local minimum, CDAT (purple) reaches the global minimum via self-inhibition (red) that repels the state from shallow traps and topology-aware aggregation (gray) that steers it with structural priors.

standard graph benchmarks. Furthermore, we provide a dissipation analysis proving that the system dynamics monotonically minimize the energy functional and converge to a stable invariant set.

- By operationalizing the equivalence between self-attention and the mixture of von Mises–Fisher (Mo–vMF) distribution, we formulate a Mo–vMF energy to drive rapid, coarse semantic alignment in the directional feature space. This is coupled with a Hopfield refinement energy for late-stage prototype retrieval and sharpening, establishing a clear division of computational roles along the relaxation trajectory.
- We empirically demonstrate that CDAT achieves state-of-the-art performance across multiple benchmarks in graph anomaly detection and classification. It consistently outperforms strong energy-based baselines, validating that our controlled dynamics significantly enhance structural discriminability and detection stability against noise.

## 2. Related Work

**Associative memory model.** Dense associative memory networks can be viewed as a powerful generalization of the classical Hopfield network. They embed Hopfield-type dynamics into deep networks via energy-based associative memory mechanisms, thereby defining a continuous artificial recurrent neural network whose state is characterized by a vector evolving over time according to a nonlinear update rule (Millidge et al., 2022; Hoover et al., 2024; Hu et al.,

2023). Within this framework, each stored pattern exerts a “force” on the state (or particle) in a way that follows a specific statistical model. Beyond the classical capacity limitations of discrete Hopfield memories (Hopfield, 1982), dense variants substantially increase memory capacity and strengthen pattern completion by using rapidly growing nonlinearities / higher-order interactions (Krotov & Hopfield, 2016; Demircigil et al., 2017; Lucibello & Mézard, 2024), and theoretical analyses further characterize the large-capacity regime (Krotov & Hopfield, 2021; Hu et al., 2024). These developments motivate viewing representation learning through an attractor-memory lens; CDAT builds on this perspective but targets controllable and structure-aware attractor geometry for iterative inference.

### Energy-based Transformer and iterative inference.

Energy-based self-attention recasts the Transformer block as a differentiable dynamical system minimizing a global energy function (Ramsauer et al., 2021). Rather than performing a single-step weighted sum, tokens evolve self-consistently in an energy landscape, reflecting internal information flow and the relaxation of the system towards equilibrium. This view connects attention to modern Hopfield retrieval (Ramsauer et al., 2021; Bricken & Pehlevan, 2021; Sun et al., 2025; Wu et al., 2025) and motivates architectures that perform inference by iterating within a block until (approximate) convergence (Du et al., 2022; Hoover et al., 2023). Relatedly, associative memory dynamics have been used as an end-to-end differentiable solver for prototype-style objectives such as clustering (Saha et al., 2023). CDAT follows this iterative-inference paradigm but introduces a two-energy decomposition (Mo-vMF alignment vs. Hopfield refinement) and a topology-conditioned modulation to improve convergence under heterogeneous relational interactions.

**Continuous attractors and excitation–inhibition mechanisms.** Neural field models with local excitation and global inhibition can sustain continuous attractors (Amari, 1977; Wu et al., 2016; Chandra et al., 2025). Additional mechanisms such as spike-frequency adaptation can enhance tracking behavior and modulate attractor dynamics (Mi et al., 2014). CDAT leverages excitation–inhibition as a structure-dependent modulation to reshape attractor basins and suppress spurious convergence, without requiring an exact continuous-attractor manifold.

## 3. CDAT Dynamics of Token Updates

In this section, we formalize CDAT as a continuous-time dynamical system. By starting with an energy-gradient drive, we augment the trajectory with CANN-inspired excitation–inhibition dynamics to enable topology-aware modulation. We establish a dissipation certificate for the proposed

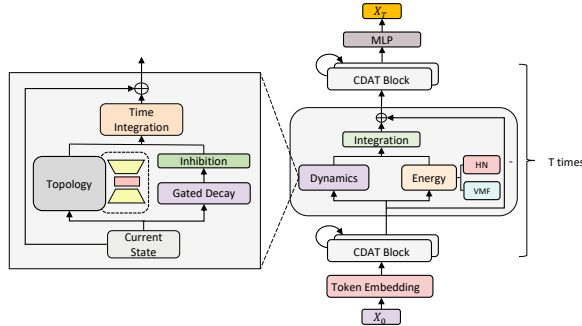


Figure 2. Overall architecture of CDAT.

dynamics via a trajectory-wise storage functional, and discretize the resulting Ordinary Differential Equation (ODE) with a first-order Euler step to obtain the CDAT update rule. The specific semantic energy used is defined in Sec. 4 and the overall architecture of CDAT is shown in Fig. 2.

### 3.1. Energy-guided Gradient Flow

AM models achieve content-addressable retrieval by pairing an explicit energy function with attractor dynamics (Krotov & Hopfield, 2021; Millidge et al., 2022): minima of the energy correspond to stable memories, and inference proceeds by driving the state toward attractors with low energy. In the same spirit of energy-based inference, we view token refinement as continuous-time *state evolution* on an energy landscape. In a  $D$ -dimensional Euclidean space, consider a state  $\mathbf{x} = (x_1, \dots, x_D) \in \mathbb{R}^D$  and  $\mathbf{g} = (g_1, \dots, g_D) \in \mathbb{R}^D$  as its layer-normalized output. Particularly let  $E : \mathbb{R}^{N \times D} \rightarrow \mathbb{R}$  be a differentiable energy function defined over this normalized state matrix  $G = [\mathbf{g}_1, \dots, \mathbf{g}_N]^T \in \mathbb{R}^{N \times D}$ . The attractor dynamics controls the trajectory of  $\mathbf{x}$  in latent space by specifying  $d\mathbf{x}/dt$ ; Under monotone energy decrease, that is  $dE/dt < 0$ , it guarantees stable convergence to a local minimum of the energy landscape. We write this as the gradient-flow ODE:

$$\tau \frac{d\mathbf{x}}{dt} = -\nabla_{\mathbf{g}} E, \quad (1)$$

where  $\tau > 0$  sets the time scale and lower energy corresponds to more compatible configurations. This establishes a principled baseline dynamics on which we introduce the controlled excitation–inhibition modulation in the next subsection.

### 3.2. Discretized Dynamic Mechanisms

While the gradient flow in Equation (1) provides a fast route to a nearby local energy minimum, its trajectory is fully dictated by the local geometry of  $E$ . As the data and interactions become more complex, the resulting energy landscape

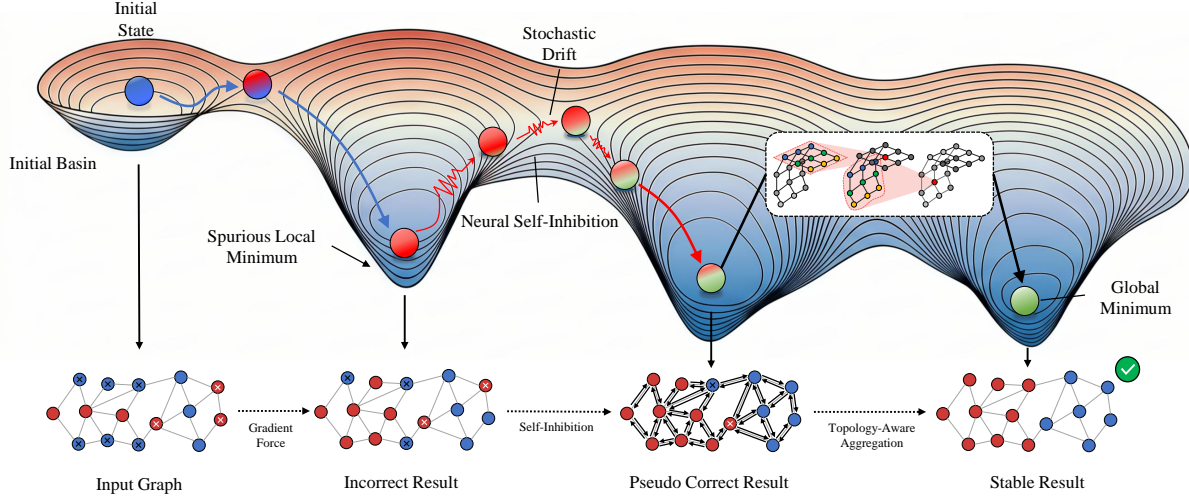


Figure 3. Demonstration of Dynamics. Illustration of the classification trajectory, with the system state (the small sphere) evolving across the energy surface. The diagram depicts an initial descent into a Spurious Local Minimum (incorrect class), followed by an escape mechanism driven by Neural Self-Inhibition and Stochastic Drift (red wavy arrows). These terms propel the state through a pseudo-correct basin and, via Topology-Aware Updates, into the True Classification Basin (global minimum) for the correct stable result.

can become sharply curved and brittle, making the energy design increasingly delicate and prone to abrupt capacity collapse in associative memories (Sharma et al., 2022). Based on the observations above, we use a complementary strategy: instead of relying solely on shaping  $E$ , we seek a more controllable attractor dynamics that can steer states of all objects  $X = [\mathbf{x}_1, \mathbf{x}_2, \dots, \mathbf{x}_N]^T \in \mathbb{R}^{N \times D}$  toward better basins through explicit excitation–inhibition regulation. We therefore instantiate the drift field by augmenting the energy-gradient drive with decay, topology-conditioned coupling, and adaptive self-inhibition. For clarity, we present the dynamics for a single token state  $\mathbf{x}(t)$  by

$$\tau \frac{d\mathbf{x}}{dt} = -\mathbf{x} + W\mathbf{x} - \omega\mathbf{x} - \nabla_{\mathbf{g}} E. \quad (2)$$

Equation (2) decomposes the drift into four terms: a passive decay  $-\mathbf{x}$ , a topology-dependent excitation term parameterized by  $W \in \mathbb{R}^{D \times D}$ , a global damping term  $-\omega\mathbf{x}$  where  $\omega \in \mathbb{R}_{>0}$  is a learnable scalar decay parameter and the task-directed energy drive  $-\nabla_{\mathbf{g}} E$ . Together, these terms define a controllable attractor dynamics that improves basin search while retaining stable convergence.

**Topology-conditioned mutual excitation  $W\mathbf{x}$ .** For structured token interactions, an analogous construction can be achieved by defining a distance-based coupling kernel over an interaction structure. Concretely, let feature dimensions be indexed by  $\mathcal{D} = \{1, \dots, D\}$  and endow  $\mathcal{D}$  with a task-dependent distance  $d: \mathcal{D} \times \mathcal{D} \rightarrow \mathbb{R}_{\geq 0}$ . Thus, we parameterize the coupling matrix  $W_{ij}$  by decomposing it into a

fixed geometric prior and a learnable residual, *i.e.*

$$W_{ij} = J_0 \exp\left(-\frac{d(i, j)^2}{2a^2}\right) + W_{ij}^{\text{train}}, \quad (3)$$

where the Gaussian term imposes a locality bias, with  $J_0$  scaling the excitation strength and  $a$  controlling the receptive range;  $W_{ij}^{\text{train}}$  provides a global correction for long-range dependencies. Crucially, the coupling is heterogeneous in feature space: the neighborhood structure induced by  $d(i, j)$  is generally non-uniform across dimensions, which breaks the translation-like symmetry required for continuous attractors. As a result, activity bumps are no longer equivalent under shifts on the feature manifold; instead they become biased toward structurally preferred regions (*i.e.*, dimensions with denser or stronger effective couplings), yielding a finite set of stable fixed points rather than a continuum of equivalent states (Seeholzer et al., 2019).

**Global damping  $-\omega\mathbf{x}$  for energy dissipation and stabilization.** The self-inhibition term  $-\omega\mathbf{x}$  can be viewed as a coarse linear model of spike-frequency adaptation (SFA), implementing a delayed negative-feedback loop whereby sustained activity elicits an opposing inhibitory current that counteracts excitation (Gutkin & Zeldenrust, 2014). From a dynamical systems perspective, such negative feedback can destabilize spatially localized steady-state attractors. As shown in Fig. 3, in the context of energy landscape optimization, the resulting intrinsic velocity plays a role analogous to inertial momentum: when the trajectory becomes trapped in shallow local minima, accumulated activity generates a

repulsive effect that pushes the state away from its current location (Mi et al., 2014). Consequently, self-inhibition facilitates barrier crossing and promotes convergence toward deeper minima that correspond to the true class centers.

### 3.3. Euler Discretization and Layerwise Interpretation

As discussed above, CDAT goes beyond plain negative-gradient descent by introducing a controlled, higher-order dynamical system that governs trajectory evolution, rather than merely shaping the energy landscape. While the design is grounded in classical excitation–inhibition attractor mechanisms, our goal is not to reproduce a specific CANN model (Amari, 1977), but to expose a control interface that is both principled and implementation-friendly.

In this view, the resulting discretized updates map directly to modern deep architectures. The excitation term corresponds to an additional structural mixing layer, while the inhibition term behaves like an extra pointwise transformation on the updated state. To make this connection explicit, we define the step size  $\alpha := \Delta t/\tau$  and apply a first-order (Euler) discretization to the dynamics in Equation (2), yielding the state evolution of  $\mathbf{x}$  at step  $t$  as

$$\mathbf{x}^{t+\Delta t} = \mathbf{x}^t + \alpha \cdot \left[ W \cdot \mathbf{x}^t - (\omega + 1)\mathbf{x}^t - \nabla_{\mathbf{g}} E^t \right]. \quad (4)$$

We next establish a theoretical link between the proposed neurodynamics and modern neural networks. In particular, we show that the Euler-discretized evolution is isomorphic to a residual convolutional layer (LeCun et al., 2002) with a strong local-connectivity inductive bias. This viewpoint unifies message passing on graphs and convolution on grids as two instances of the same operator form.

**Theorem 3.1** (Excitation increment as residual convolution). *Consider the Euler-discretized update of the proposed dynamics (4). When the coupling matrix  $W$  in the mutual-excitation term is instantiated using the kernel-based parametrization in (3), the resulting mutual-excitation increment  $\alpha W \mathbf{x}^t$  implements a feature-space convolution, corresponding to a globally parameterized aggregation operator defined by  $W$ . This structure naturally induces a ResCNN-style residual update, i.e.,*

$$\mathbf{x}^{t+\Delta t} = \underbrace{\mathbf{x}^t}_{\text{Residual}} + \underbrace{\alpha W \mathbf{x}^t}_{\text{Convolution}}. \quad (5)$$

Theorem 3.1 establishes an explicit correspondence between the Euler-discretized dynamics and a feature-space convolutional update: the mutual-excitation term instantiates aggregation through a Gaussian heat-kernel operator, further modulated by learnable coupling weights. See Appendix E.1 for the proof.

### 3.4. Dissipation Analysis

To certify the dissipative structure of the modified dynamics (Equation (2)), we introduce the following storage functional along trajectory as

$$V(t) = E(\mathbf{g}(t)) + \int_{t_0}^t \left( ((1+\omega)\mathbf{x}(s) - W\mathbf{x}(s))^\top \dot{\mathbf{g}}(s) \right) ds, \quad (6)$$

where  $\mathbf{g}(t) = \mathbf{g}(\mathbf{x}(t))$  for brevity;  $t_0$  is an arbitrary initial time. The integral is well-defined since  $\mathbf{x}(\cdot)$  and  $\mathbf{g}$  are continuously differentiable functions of one order, hence  $\dot{\mathbf{g}}(\cdot)$  is continuous. We next establish the key Jacobian property in Lemma 3.2 (Tang & Kopp, 2021; Krotov, 2021) before proving dissipation.

**Lemma 3.2** (LayerNorm Jacobian is PSD). *Let  $\mu(\mathbf{x})$  and  $\sigma(\mathbf{x})$  be the mean and standard deviation over  $\mathbf{x} \in \mathbb{R}^D$ , with*

$$\sigma(\mathbf{x}) = \sqrt{\frac{1}{D} \|\mathbf{x} - \mu(\mathbf{x}) \cdot \mathbf{1}\|_2^2 + \varepsilon}, \quad \varepsilon > 0,$$

where  $\mathbf{1} \in \mathbb{R}^D$  is the all-ones vector. For  $\mathbf{g}(\mathbf{x}) = \gamma \frac{\mathbf{x} - \mu(\mathbf{x}) \cdot \mathbf{1}}{\sigma(\mathbf{x})}$  with  $\gamma > 0$ , its Jacobian matrix  $M(\mathbf{x}) = \nabla_{\mathbf{x}} \mathbf{g}(\mathbf{x})$  is symmetric positive semidefinite.

**Theorem 3.3** (Dissipation certificate for the modified dynamics). *Let  $\mathbf{x}(t)$  be any solution of dynamics*

$$\tau \dot{\mathbf{x}} = -\mathbf{x} + W\mathbf{x} - \omega\mathbf{x} - \nabla_{\mathbf{g}} E,$$

with  $W^\top = W$ . Suppose  $\mathbf{g}$  represents the Layer-normalized output of  $\mathbf{x}$  as defined in Lemma 3.2. Then the trajectory-wise storage functional  $V(t)$  for any fixed  $t_0$  as Equation (6) is non-increasing, i.e.,

$$\frac{d}{dt} V(t) = -\tau \dot{\mathbf{x}}(t)^\top M(\mathbf{x}(t)) \dot{\mathbf{x}}(t) \leq 0, \quad (7)$$

where  $M(\mathbf{x}(t)) = \nabla_{\mathbf{x}} \mathbf{g}(\mathbf{x}(t))$  is the Jacobian matrix of  $\mathbf{g}$ .

The monotonic decrease of  $V(t)$  establishes that the proposed dynamics is energy-dissipative. As in prior work on Associative Memory models (Saha et al., 2023), we use this property to characterize the attractor structure of the dynamics. A detailed proof is deferred to Appendix E.2.

#### Symmetric, low-rank parameterization of the coupling.

The dissipation result in Theorem 3.3 assumes a symmetric coupling  $W = W^\top$ . This is both theoretically and practically motivated. Theoretically, symmetry aligns the mutual-excitation term with an energy-based interaction and avoids non-conservative rotational components. On the implementation side, we enforce symmetry by parameterizing

$$W = P^\top QP, \quad (8)$$

where  $P \in \mathbb{R}^{r \times D}$  with  $r \ll D$ ;  $Q \in \mathbb{R}^{r \times r}$  is diagonal (or block-diagonal). By construction,  $W$  is symmetric, and its rank is at most  $r$  when  $Q$  is full-rank. This yields a parameter-efficient update rule reminiscent of LoRA: the mutual-excitation operator is obtained from a low-dimensional bottleneck  $P$  and a lightweight scaling  $Q$ , reducing the number of free parameters from  $\mathcal{O}(D^2)$  to  $\mathcal{O}(rD)$  while retaining expressive, learnable couplings (Hu et al., 2022). In our experiments, this constraint stabilizes training and improves the robustness of the controlled dynamics.

#### 4. Associative Memories for CDAT

The controlled dynamics established in Section 3 (Equation (2)) are driven by the gradient of a semantic potential,  $-\nabla_g E$ . In this section, we instantiate this energy  $E$  to explicitly guide tokens toward consistent configurations via two complementary forces: input-conditioned alignment and prototype-based refinement. Given states  $X \in \mathbb{R}^{N \times D}$  and relational structure  $\mathcal{G}$ , we define the semantic energy of CDAT as

$$E(X; \mathcal{G}) = \lambda_v E^{\text{ATT-vMF}}(X) + \lambda_h E^{\text{HN}}(X), \quad (9)$$

where  $E^{\text{ATT-vMF}}$  induces directional semantic alignment via a Mo-vMF interpretation of self-attention, and  $E^{\text{HN}}$  implements Hopfield-type prototype retrieval and sharpening.  $\lambda_v$  and  $\lambda_h$  represent the balancing weights, satisfying  $\lambda_v + \lambda_h = 1$ .

##### 4.1. Mo-vMF Term $E^{\text{ATT-vMF}}$ : Self-attention as Directional Mixture Modeling

Energy-based self-attention (Ramsauer et al., 2021) casts a Transformer attention block as minimizing an explicit energy function. This interpretation motivates us to treat token interactions as a differentiable dynamical system parameterized by the usual query/key projections. Consider a state vector  $\mathbf{x}$  and its LayerNorm-normalized output  $\mathbf{g}$ . For each head  $h \in \{1, \dots, H\}$ , we obtain query and key vectors by linearly embedding  $\mathbf{g}$  into an internal feature space of dimension  $Y$  via learnable tensors  $\mathbf{W}^Q, \mathbf{W}^K \in \mathbb{R}^{Y \times H \times D}$ . The query and key vectors are obtained as

$$Q_{hi} = \frac{\mathbf{W}_h^Q \mathbf{g}_i}{\|\mathbf{W}_h^Q \mathbf{g}_i\|_2}, \quad K_{hi} = \frac{\mathbf{W}_h^K \mathbf{g}_i}{\|\mathbf{W}_h^K \mathbf{g}_i\|_2}. \quad (10)$$

The energy of the attention mechanism is defined as

$$E^{\text{ATT-vMF}} = -\frac{1}{\beta} \sum_{h=1}^H \sum_{C=1}^N \log \left( \sum_{B \neq C} \exp(\beta Q_{hB}^\top K_{hC}) \right). \quad (11)$$

We connect the log-sum-exp term in  $E^{\text{ATT-vMF}}$  to a probabilistic mixture model on the unit sphere  $S^{Y-1} = \{l \in \mathbb{R}^Y :$

$\|l\| = 1\}$ . The von Mises–Fisher distribution on  $S^{Y-1}$  with mean direction  $\mu \in S^{Y-1}$  and concentration  $\beta$  has density

$$p_{\text{vMF}}(q | \mu, \beta) = c_Y(\beta) \exp(\beta \mu^\top q), \quad (12)$$

where  $q \in S^{Y-1}$  and  $c_Y(\beta)$  is a normalizing constant depending only on  $(Y, \beta)$ . Thus, Mo-vMF with shared concentration  $\beta$  is

$$p_{\text{Mo-vMF}}(q) = \sum_{b=1}^M \pi_b p_{\text{vMF}}(q | \mu_b, \beta), \quad (13)$$

where  $\pi_b \geq 0$ ,  $\sum_{b=1}^M \pi_b = 1$ , and  $\mu_b \in S^{Y-1}$  for all  $b$ .

**Theorem 4.1** (Self-attention energy as a Mo-vMF negative log-likelihood). *Consider single-head self-attention situation with normalized query and key vectors  $Q_B, K_C \in S^{Y-1}$ , we define the attention energy with  $\beta > 0$  as*

$$E^{\text{ATT-vMF}} = -\frac{1}{\beta} \sum_{C=1}^N \log \left( \sum_{B \neq C} \exp(\beta Q_B^\top K_C) \right). \quad (14)$$

Then, ignoring constant terms independent of  $\{Q_B, K_C\}$ ,  $E^{\text{ATT-vMF}}$  is equivalent to the negative log-marginal likelihood of a Mo-vMF model on the hypersphere  $S^{Y-1}$  with shared concentration  $\beta$ .

Theorem 4.1 connects attention to directional mixture modeling, where query vectors act as mixture directions and updates encourage angular alignment. A formal statement and proof are deferred to Appendix E.3.

We emphasize that the Mo-vMF interpretation serves as a geometric prior defining the attractor basins. While consistent with recent insights (Schaeffer et al., 2023), our contribution lies in operationalizing this equivalence to shift the modeling perspective: from implicit energy descent to explicit probabilistic evolution. This theoretical grounding justifies the decomposition in Equation (9), ensuring that the coarse alignment is driven by a rigorous spherical mixture prior.

##### 4.2. Hopfield Refinement Term $E^{\text{HN}}$ : Prototype Retrieval and Sharpening

Mo-vMF analysis suggests that self-attention can be viewed as dynamically modeling directional similarity among inputs on a spherical manifold, yielding a form of continuous, input-driven self-organization. Furthermore, we introduce a Hopfield energy  $E^{\text{HN}}$  to enforce global structural consistency. Unlike the adaptive prototypes in Mo-vMF, this term anchors the dynamics to a set of fixed, learnable memory patterns, providing stable attractors for the trajectory (Hopfield, 1982; Krotov & Hopfield, 2016). Concretely, a modern Hopfield-type energy can be written by

$$E^{\text{HN}} = -\sum_{B=1}^N \sum_{\mu=1}^P \text{ReLU} \left( \sum_{j=1}^D \xi_{\mu j} g_{jB} \right), \quad (15)$$

Table 1. Graph classification performance on seven benchmarks (higher is better). Following (Morris et al., 2020), means and standard deviations over 100 runs of 10-fold cross-validation are reported. Abbreviation: MUTAGEN. = MUTAGENICITY.

Method	PROTEINS	NCI1	NCI109	DD	ENZYMES	MUTAG	MUTAGEN.
WKPI (k-means)	78.5±0.4	87.5±0.5	85.9±0.4	82.0±0.3	—	85.8±2.5	—
GRDL	82.6±1.2	80.4±0.8	—	—	—	92.1±5.9	—
DSGCN	77.3±0.4	—	—	—	78.4±0.6	—	—
Norm-GN	—	84.9±1.7	83.5±1.3	—	73.3±8.0	—	—
GIN + GraphNorm	77.4±4.9	81.4±2.4	82.4±1.7	—	—	91.6±6.5	—
GIN + GRANOLA	77.5±3.7	84.0±1.7	83.7±1.6	—	—	92.2±4.6	—
HGP-SL	84.9±1.6	78.5±0.8	80.7±1.2	81.0±1.3	68.8±2.1	—	82.2±0.6
HGP	79.4±3.1	74.2±1.7	—	72.8±5.4	44.5±7.4	87.9±5.7	77.9±1.4
ASAP	74.2±0.8	71.5±0.4	70.1±0.6	76.9±0.7	—	—	—
MinCutPool	74.7±0.5	74.3±0.9	—	—	—	90.6±4.6	—
U2GNN	80.0±3.2	—	—	—	95.7±1.9	—	88.5±7.1
Graphormer	76.3±2.7	78.6±2.1	—	—	—	89.6±6.2	—
ET	<b>90.3±0.7</b>	<u>90.1±0.1</u>	<u>90.5±0.1</u>	<u>95.9±0.8</u>	<b>99.8</b>	<u>96.6±0.2</u>	<u>98.7±0.1</u>
<b>CDAT (ours)</b>	<u>87.1±0.4</u>	<b>93.5±0.2</b>	<b>94.3±0.1</b>	<b>98.5±0.6</b>	<u>99.1±0.1</u>	<b>98.8±0.3</b>	<b>98.8±0.1</b>

where  $\{\xi_\mu\}_{\mu=1}^P \in \mathbb{R}^{P \times D}$  denote learnable global stored memory vectors. From a dynamical systems perspective, this energy landscape exhibits  $P$  local minima, each corresponding to a stored memory pattern. Overall,  $E^{\text{HN}}$  acts as a late-stage refinement mechanism: it performs prototype-style retrieval and sharpening, progressively dominating the trajectory as the system approaches stable attractors.

## 5. Empirical Evaluation

Although the CDAT formulation is general and applies to any tokenized relational data, we focus on the graph domain as a principled and challenging testbed. Graph representation learning requires simultaneously preserving local structural fidelity, integrating global context, and remaining robust to noisy features and perturbations (Hamilton et al., 2017; Wu et al., 2021). Classic message-passing models such as GCNs (Kipf & Welling, 2017) and their variants usually suffer from over-smoothing at depth, while attention-based graph models (e.g., GAT (Veličković et al., 2018)) may over-globalize interactions or face scalability issues. These challenges make graphs a natural benchmark for studying whether energy-based attractor dynamics can stabilize learning and improve discriminability.

In following sections, we empirically validate the CDAT’s benefits on standard graph learning tasks. We conduct extensive experiments on both graph-level classification and graph anomaly detection tasks to comprehensively evaluate the effectiveness of the proposed CDAT. Overall, CDAT demonstrates consistent and competitive performance across diverse datasets. The code is available at

<https://github.com/Angelov1vil/CDAT>.

### 5.1. Graph Classification with CDAT

We compare CDAT with the current state of the art approaches for the mentioned datasets, which include GRDL (Wang & Fan, 2024), GRANOLA (Eliasof et al., 2024), ET (Hoover et al., 2023), DSGCN (Balcilar et al., 2020), HGP-SL (Zhang et al., 2021). Additionally, approaches (Yang et al., 2022; Orsini et al., 2015; Ranjan et al., 2020; Zhao & Wang, 2019; Cai et al., 2021; Nguyen et al., 2022; Bianchi et al., 2020), which are close to the baselines, are included to further contrast the performance of our model. The results are summarized in Table 1.

Across seven widely used datasets, CDAT achieves state-of-the-art performance on 5 out of 7 datasets. Specifically, CDAT yields significant absolute accuracy gains over ET, improving by 3.4% on NCI1, 3.8% on NCI109, and 2.2% on MUTAG. On the challenging DD dataset, CDAT not only surpasses ET by 2.6% but also demonstrates overwhelming dominance over classical pooling methods (e.g., exceeding HGP-SL by >13%), highlighting its capability to capture complex structural dependencies. While ET remains competitive on PROTEINS, CDAT’s superior performance across the majority of benchmarks confirms that our attractor dynamics provide a more expressive and stable inductive bias than naive energy descent.

Notably, the gains are most pronounced on structurally complex datasets such as DD (284 avg. nodes) and the NCI family, where heterogeneous relational interactions demand richer aggregation beyond what plain energy minimization

Table 2. Performance on Yelp, Amazon, and T-Finance across different training ratios. Means and standard deviations (when available from prior work) are reported over five runs with varying train/dev/test splits. Best results are in bold; second-best are underlined.

Metric	Datasets	Split	CAREGNN	PC-GNN	BWGNN	GT	ET	UniGAD	CDAT
MF1	Yelp	1%	62.1±1.3	59.8±1.4	61.1±0.4	61.7±0.4	<u>62.7±1.9</u>	–	<b>63.0±1.4</b>
	Yelp	40%	63.3±0.9	63.0±2.3	<b>71.0±0.9</b>	68.7±0.4	69.5±0.2	–	<u>70.5±0.1</u>
	Yelp	70%	–	–	–	–	<u>70.3±0.4</u>	70.2	<b>71.5±0.2</b>
	Amazon	1%	68.7±1.6	79.8±5.6	<u>90.9±0.7</u>	88.6±0.5	89.3±0.7	–	<b>91.2±0.9</b>
	Amazon	40%	86.3±1.7	85.0±0.7	<b>92.2±0.4</b>	91.7±0.8	90.4±1.0	–	<u>92.1±0.6</u>
	Amazon	70%	–	–	–	–	<b>92±0.3</b>	91.3	<u>91.9±0.1</u>
	T-Finance	1%	73.3	62.0	<u>86.8</u>	81.5	85.1±1.0	–	<b>87.4±1.1</b>
	T-Finance	40%	77.5	63.1	86.8	83.6	88.2±1.0	<u>89.75</u>	<b>90.6±0.6</b>
	AUC	Yelp	1%	<u>75.0±3.8</u>	<b>75.4±0.9</b>	72.0±0.5	72.5±0.6	72.9±1.3	–
Yelp		40%	<u>76.1±2.9</u>	79.8±0.1	<u>84.0±0.9</u>	81.9±0.5	83.6±2.8	–	<b>84.4±0.2</b>
Yelp		70%	–	–	–	–	81.7±1	<u>86.23</u>	<b>91.9±0.3</b>
Amazon		1%	88.6±3.5	90.4±2.0	89.4±0.3	89.0±1.2	<u>91.9±1.0</u>	–	<b>94.5±1.1</b>
Amazon		40%	90.5±1.6	95.8±0.1	<b>98.0±0.4</b>	95.4±0.6	95.7±2.0	–	<u>97.2±0.2</u>
Amazon		70%	–	–	–	–	<u>97.1±2.1</u>	<b>97.84</b>	93.0±5.0
T-Finance		1%	90.5	90.7	91.1	90.0	<u>92.2±1.1</u>	–	<b>95.91±0.4</b>
T-Finance		40%	92.1	91.2	94.3	88.2	95.0±3.0	<u>96.49</u>	<b>97.84±1.1</b>

Table 3. Ablation on the bottleneck rank  $r$  in  $W = P^\top QP$  on DD and NCI1. Accuracy (%), mean  $\pm$  std over 100 runs of 10-fold CV) is reported. “Without  $W$ ” removes the mutual-excitation term; “Full-rank  $W$ ” uses an unconstrained  $W \in \mathbb{R}^{D \times D}$  without symmetric or low-rank constraints.

Config	DD	NCI1
Without $W$	83.1 $\pm$ 2.1	82.8 $\pm$ 0.5
$r = 1$	82.2 $\pm$ 4.8	87.6 $\pm$ 0.3
$r = 2$	89.2 $\pm$ 4.1	90.2 $\pm$ 1.1
$r = 4$ (default)	<b>98.5 <math>\pm</math> 0.6</b>	<b>93.5 <math>\pm</math> 0.2</b>
$r = 8$	97.6 $\pm$ 1.3	77.0 $\pm$ 0.7
$r = 16$	97.8 $\pm$ 0.2	77.5 $\pm$ 1.2
Full rank $W$	98.0 $\pm$ 0.1	82.9 $\pm$ 0.4

can offer. This suggests that the topology-conditioned excitation–inhibition modulation is especially beneficial when graph structure is dense and varied. On smaller or simpler benchmarks such as PROTEINS, the margin narrows, which we attribute to reduced structural heterogeneity rather than a fundamental limitation of the proposed dynamics.

## 5.2. Graph Anomaly Detection with CDAT

We evaluate CDAT on graph anomaly detection following established protocols on Yelp, Amazon and T-Finance. Both MF1 and AUC are reported under varying labeled anomaly ratios. Full results are given in Table 2. CDAT achieves state-

of-the-art performance across benchmarks, with substantial gains over strong baselines and recent methods (Lin et al., 2024; Dou et al., 2020; Liu et al., 2021; Tang et al., 2022; Dwivedi & Bresson, 2020; Hoover et al., 2023). Notably, in the challenging low-label regime (1% split), CDAT outperforms ET with AUC improvements of 2.6% on Amazon and 3.7% on T-Finance. Moreover, CDAT shows superior robustness over UNIGAD in complex environments. On the dense Yelp dataset (70% split), it surpasses UNIGAD by 5.6% in AUC (91.9% vs. 86.23%) while also achieving a higher MF1 score. Similar dominance holds on T-Finance, where CDAT consistently outperforms UNIGAD across both metrics. These results highlight the advantage of modeling anomaly detection as a structured dynamical evolution process rather than a purely static scoring problem. The combination of mutual excitation and self-inhibition allows CDAT to better separate anomalous patterns from normal graph structures, leading to improved detection accuracy under challenging supervision constraints.

## 5.3. Ablation on Topology-conditioned Mutual Excitation $W$

To clarify the functional role of the coupling operator  $W$  and to validate its symmetric low-rank parameterization in Equation (8), we conduct an ablation on two representative graph classification benchmarks (DD and NCI1). Concretely, we probe how the bottleneck rank  $r$  in  $W = P^\top QP$  governs the trade-off between expressiveness and generalization by

Table 4. Wall-clock and parameter comparison on NCI109. Percentages in parentheses denote the relative overhead of CDAT over ET.

Metric	GT	ET	CDAT (ours)
Params	1.074 M	1.058 M	1.060 M
Inference (ms/batch)	$1.46 \pm 0.05$	$6.35 \pm 0.60$	$6.50 \pm 0.90$
Training (s/epoch)	$0.753 \pm 0.097$	$2.034 \pm 0.186$	$2.046 \pm 0.157$

sweeping  $r \in \{1, 2, 4, 8, 16\}$ . To delimit the two extremes of this spectrum, we further include a variant that removes  $Wx$  entirely, corresponding to the zero-capacity limit, and an unconstrained full-rank parameterization that drops both the symmetric and the low-rank constraints, corresponding to the maximum-capacity limit. All results are reported in Table 3, from which three observations emerge along this capacity spectrum. At the zero-capacity limit, removing  $Wx$  entirely drops accuracy from 98.5% to 83.1% on DD and from 93.5% to 82.8% on NCI1, confirming that the feature-coordinate couplings contribute structural priors that the semantic energies alone cannot recover. At the maximum-capacity limit, by contrast, accuracy on NCI1 degrades sharply once  $r > 4$  and the unconstrained full-rank parameterization ( $\sim 251K$  extra parameters) collapses to 82.9%; this indicates that excess capacity introduces spurious feature-dimension couplings prone to overfitting, empirically validating  $W = P^T QP$  as a principled regularizer that suppresses such modes. Between these two extremes,  $r = 4$  emerges as a robust default, delivering the best accuracy on both benchmarks with only 2,020 parameters (0.19% of the total model budget), and is therefore adopted throughout our experiments.

Notably, the full-rank configuration remains competitive on DD (98.0%) but degrades substantially on NCI1 (82.9%). This shows that enforcing the symmetry of  $W$  does not bottleneck performance; rather, the symmetric low-rank parameterization serves as a principled inductive bias that stabilizes training while preserving the dissipative structure required by Theorem 3.3.

#### 5.4. Inference Cost and Runtime Comparison

To quantify the computational overhead introduced by our formulation, we conduct a controlled wall-clock comparison on the NCI109 dataset against ET (Hoover et al., 2023) and GT (Dwivedi & Bresson, 2020) baselines, keeping all other settings (batch size, hardware, precision, optimizer) identical. Results are averaged over 5 runs and reported as mean  $\pm$  std in Table 4. We observe that CDAT and ET exhibit essentially identical computational cost: the additional parameters introduced by our design account for only +0.19%, and inference latency increases by just +2.4%. This confirms that our modifications do not meaningfully alter the computational profile of the energy-based

paradigm. The feed-forward GT baseline achieves lower latency through single-pass execution, but at the cost of substantially weaker task performance (see Table 2). This latency is intrinsic to the iterative relaxation paradigm underlying energy-based models and is not introduced by CDAT.

## 6. Limitations and Future Work

In this paper, we present CDAT, an energy-based framework incorporating CANN-inspired dynamics to stabilize inference trajectories. While CDAT achieves state-of-the-art graph classification and anomaly detection by suppressing spurious local minima, its iterative state unfolding incurs higher inference costs than standard feed-forward Transformers. To address this, future work will focus on learning a more expressive control interface, such as state-dependent schedules for damping parameter  $\omega$ , to optimize the trade-off between convergence speed and robustness. Furthermore, we plan to extend the framework with richer semantic energy landscapes—beyond standard Mo-vMF and Hopfield energies by incorporating multi-prototype hyperspherical energies and task-adaptive energy families. Finally, given CDAT’s structural flexibility, we intend to deploy it as a specialized substructure within larger hierarchical architectures, validating its versatility akin to (Cao et al., 2025; Zhuge et al., 2025).

## Acknowledgments

This work is supported by the Fundamental and Interdisciplinary Disciplines Breakthrough Plan of the Ministry of Education of China (No. JYB2025XDXM101), the National Natural Science Foundation of China (No. 62272374), the Natural Science Foundation of Shaanxi Province (No.2024JC-JCQN-62), the State Key Laboratory of Communication Content Cognition under Grant No. A202502, and the Key Research and Development Project in Shaanxi Province (No. 2023GXLH-024).

## Impact Statement

This paper presents work whose goal is to advance the field of Machine Learning. There are many potential societal consequences of our work, none which we feel must be specifically highlighted here.

## References

- Amari, S.-i. Dynamics of pattern formation in lateral-inhibition type neural fields. *Biological Cybernetics*, 27(2):77–87, 1977.
- Amit, D. J. *Modeling brain function: The world of attractor neural networks*. Cambridge university press, 1989.
- Amit, D. J., Gutfreund, H., and Sompolinsky, H. Storing infinite numbers of patterns in a spin-glass model of neural networks. *Physical Review Letters*, 55(14):1530, 1985.
- Balcilar, M., Renton, G., Héroux, P., Gauzere, B., Adam, S., and Honeine, P. Bridging the gap between spectral and spatial domains in graph neural networks. *arXiv preprint arXiv:2003.11702*, 2020.
- Bianchi, F. M., Grattarola, D., and Alippi, C. Spectral clustering with graph neural networks for graph pooling. In *International Conference on Machine Learning*, pp. 874–883. PMLR, 2020.
- Bricken, T. and Pehlevan, C. Attention approximates sparse distributed memory. In Ranzato, M., Beygelzimer, A., Dauphin, Y., Liang, P., and Vaughan, J. W. (eds.), *Advances in Neural Information Processing Systems*, volume 34, pp. 15301–15315. Curran Associates, Inc., 2021.
- Cai, T., Luo, S., Xu, K., He, D., Liu, T.-y., and Wang, L. Graphnorm: A principled approach to accelerating graph neural network training. In *International Conference on Machine Learning*, pp. 1204–1215. PMLR, 2021.
- Cao, J., Wang, J., Wei, R., Guo, Q., Chen, K., Zhou, B., and Lin, Z. Memory decoder: A pretrained, plug-and-play memory for large language models. In *Advances in Neural Information Processing Systems*, 2025. URL <https://openreview.net/forum?id=ARJpQtLXfe>.
- Chandra, S., Sharma, S., Chaudhuri, R., and Fiete, I. Episodic and associative memory from spatial scaffolds in the hippocampus. *Nature*, 638(8051):739–751, 2025.
- Davis, J. Q., Gu, A., Choromanski, K., Dao, T., Re, C., Finn, C., and Liang, P. Catformer: Designing stable transformers via sensitivity analysis. In Meila, M. and Zhang, T. (eds.), *International Conference on Machine Learning*, volume 139 of *Proceedings of Machine Learning Research*, pp. 2489–2499. PMLR, 2021. URL <https://proceedings.mlr.press/v139/davis21a.html>.
- Demircigil, M., Heusel, J., Löwe, M., Uppgang, S., and Vermet, F. On a model of associative memory with huge storage capacity. *Journal of Statistical Physics*, 168(2): 288–299, 2017.
- Dou, Y., Liu, Z., Sun, L., Deng, Y., Peng, H., and Yu, P. S. Enhancing graph neural network-based fraud detectors against camouflaged fraudsters. In *Proceedings of the 29th ACM International Conference on Information & Knowledge Management*, pp. 315–324, 2020.
- Du, Y., Li, S., Tenenbaum, J., and Mordatch, I. Learning iterative reasoning through energy minimization. In *International Conference on Machine Learning*, pp. 5570–5582. PMLR, 2022.
- Dwivedi, V. P. and Bresson, X. A generalization of transformer networks to graphs. *arXiv preprint arXiv:2012.09699*, 2020.
- Eliasof, M., Bevilacqua, B., Schönlieb, C.-B., and Maron, H. Granola: Adaptive normalization for graph neural networks. In Globerson, A., Mackey, L., Belgrave, D., Fan, A., Paquet, U., Tomczak, J., and Zhang, C. (eds.), *Advances in Neural Information Processing Systems*, volume 37, pp. 90514–90551. Curran Associates, Inc., 2024. doi: 10.52202/079017-2873.
- Gutkin, B. and Zeldenrust, F. Spike frequency adaptation. *Scholarpedia*, 9(2):30643, 2014. doi: 10.4249/scholarpedia.30643. revision #143322.
- Hamilton, W. L., Ying, R., and Leskovec, J. Representation learning on graphs: Methods and applications. *arXiv preprint arXiv:1709.05584*, 2017.
- Hinton, G. and Anderson, J. *Parallel Models of Associative Memory: Updated Edition*. Taylor & Francis, 2014. ISBN 9781317785200. URL <https://books.google.com.sg/books?id=4w3sAgAAQBAJ>.
- Hoover, B., Liang, Y., Pham, B., Panda, R., Strobel, H., Chau, D. H., Zaki, M., and Krotov, D. Energy transformer. In Oh, A., Naumann, T., Globerson, A., Saenko, K., Hardt, M., and Levine, S. (eds.), *Advances in Neural Information Processing Systems*, volume 36, pp. 27532–27559. Curran Associates, Inc., 2023.
- Hoover, B., Chau, D. H., Strobel, H., Ram, P., and Krotov, D. Dense associative memory through the lens of random features. In Globerson, A., Mackey, L., Belgrave, D., Fan, A., Paquet, U., Tomczak, J., and Zhang, C. (eds.), *Advances in Neural Information Processing Systems*, volume 37, pp. 23549–23576. Curran Associates, Inc., 2024. doi: 10.52202/079017-0742.
- Hopfield, J. J. Neural networks and physical systems with emergent collective computational abilities. *Proceedings of the National Academy of Sciences*, 79(8):2554–2558, 1982.

- Hu, E. J., yelong shen, Wallis, P., Allen-Zhu, Z., Li, Y., Wang, S., Wang, L., and Chen, W. LoRA: Low-rank adaptation of large language models. In *International Conference on Learning Representations*, 2022. URL <https://openreview.net/forum?id=nZeVKeeFYf9>.
- Hu, J. Y.-C., Yang, D., Wu, D., Xu, C., Chen, B.-Y., and Liu, H. On sparse modern hopfield model. In Oh, A., Naumann, T., Globerson, A., Saenko, K., Hardt, M., and Levine, S. (eds.), *Advances in Neural Information Processing Systems*, volume 36, pp. 27594–27608. Curran Associates, Inc., 2023.
- Hu, J. Y.-C., Chang, P.-H., Luo, R., Chen, H.-Y., Li, W., Wang, W.-P., and Liu, H. Outlier-efficient hopfield layers for large transformer-based models. *arXiv preprint arXiv:2404.03828*, 2024.
- Kipf, T. N. and Welling, M. Semi-supervised classification with graph convolutional networks. In *International Conference on Learning Representations*, 2017. URL <https://openreview.net/forum?id=SJU4ayYgl>.
- Krotov, D. Hierarchical associative memory. *CoRR*, abs/2107.06446, 2021. URL <https://arxiv.org/abs/2107.06446>.
- Krotov, D. and Hopfield, J. J. Dense associative memory for pattern recognition. In Lee, D., Sugiyama, M., Luxburg, U., Guyon, I., and Garnett, R. (eds.), *Advances in Neural Information Processing Systems*, volume 29. Curran Associates, Inc., 2016.
- Krotov, D. and Hopfield, J. J. Large associative memory problem in neurobiology and machine learning. In *International Conference on Learning Representations*, 2021. URL [https://openreview.net/forum?id=X4y\\_100X-hX](https://openreview.net/forum?id=X4y_100X-hX).
- LeCun, Y., Bottou, L., Bengio, Y., and Haffner, P. Gradient-based learning applied to document recognition. *Proceedings of the IEEE*, 86(11):2278–2324, 2002.
- Lin, Y., Tang, J., Zi, C., Zhao, H. V., Yao, Y., and Li, J. UniGAD: Unifying multi-level graph anomaly detection. In *Advances in Neural Information Processing Systems*, 2024. URL <https://openreview.net/forum?id=sRILMnkkQd>.
- Liu, Y., Ao, X., Qin, Z., Chi, J., Feng, J., Yang, H., and He, Q. Pick and choose: a gnn-based imbalanced learning approach for fraud detection. In *Proceedings of the Web Conference 2021*, pp. 3168–3177, 2021.
- Lucibello, C. and Mézard, M. Exponential capacity of dense associative memories. *Physical Review Letters*, 132(7):077301, 2024.
- Mi, Y., Fung, C. C. A., Wong, K. Y. M., and Wu, S. Spike frequency adaptation implements anticipative tracking in continuous attractor neural networks. In Ghahramani, Z., Welling, M., Cortes, C., Lawrence, N., and Weinberger, K. (eds.), *Advances in Neural Information Processing Systems*, volume 27. Curran Associates, Inc., 2014.
- Millidge, B., Salvatori, T., Song, Y., Lukasiewicz, T., and Bogacz, R. Universal hopfield networks: A general framework for single-shot associative memory models. In *International Conference on Machine Learning*, pp. 15561–15583. PMLR, 2022.
- Morris, C., Kriege, N. M., Bause, F., Kersting, K., Mutzel, P., and Neumann, M. TUDataset: A collection of benchmark datasets for learning with graphs. *arXiv preprint arXiv:2007.08663*, 2020.
- Nguyen, D. Q., Nguyen, T. D., and Phung, D. Universal graph transformer self-attention networks. In *Companion Proceedings of the Web Conference 2022*, pp. 193–196, 2022.
- Orsini, F., Frasconi, P., De Raedt, L., Yang, Q., and Wooldridge, M. Graph invariant kernels. In *Proceedings of the twenty-fourth international joint conference on artificial intelligence*, volume 2015, pp. 3756–3762. IJCAI-INT JOINT CONF ARTIF INTELL, 2015.
- Ramsauer, H., Schäfl, B., Lehner, J., Seidl, P., Widrich, M., Gruber, L., Holzleitner, M., Adler, T., Kreil, D., Kopp, M. K., Klambauer, G., Brandstetter, J., and Hochreiter, S. Hopfield networks is all you need. In *International Conference on Learning Representations*, 2021. URL <https://openreview.net/forum?id=tL89RnzIiCd>.
- Ranjan, E., Sanyal, S., and Talukdar, P. Asap: Adaptive structure aware pooling for learning hierarchical graph representations. In *Proceedings of the AAAI conference on artificial intelligence*, volume 34, pp. 5470–5477, 2020.
- Rolls, E. T. The mechanisms for pattern completion and pattern separation in the hippocampus. *Frontiers in Systems Neuroscience*, 7:74, 2013.
- Saha, B., Krotov, D., Zaki, M. J., and Ram, P. End-to-end differentiable clustering with associative memories. In *International Conference on Machine Learning*, pp. 29649–29670. PMLR, 2023.
- Samsonovich, A. and McNaughton, B. L. Path integration and cognitive mapping in a continuous attractor neural network model. *Journal of Neuroscience*, 17(15):5900–5920, 1997.

- Schaeffer, R., Khona, M., Zahedi, N., Fiete, I. R., Gromov, A., and Koyejo, S. Associative memory under the probabilistic lens: Improved transformers & dynamic memory creation. In *Associative Memory & Hopfield Networks in 2023*, 2023. URL <https://openreview.net/forum?id=l061aZlteS>.
- Seeholzer, A., Deger, M., and Gerstner, W. Stability of working memory in continuous attractor networks under the control of short-term plasticity. *PLoS Computational Biology*, 15(4):e1006928, 2019.
- Sharma, S., Chandra, S., and Fiete, I. Content addressable memory without catastrophic forgetting by heteroassociation with a fixed scaffold. In *International Conference on Machine Learning*, pp. 19658–19682. PMLR, 2022.
- Sun, Y., Ochiai, H., Wu, Z., Lin, S., and Kanai, R. Associative transformer. In *Proceedings of the IEEE/CVF Conference on Computer Vision and Pattern Recognition*, pp. 4518–4527, June 2025.
- Tang, F. and Kopp, M. A remark on a paper of krotov and hopfield [arxiv:2008.06996], 2021. URL <https://arxiv.org/abs/2105.15034>.
- Tang, J., Li, J., Gao, Z., and Li, J. Rethinking graph neural networks for anomaly detection. In *International Conference on Machine Learning*, pp. 21076–21089. PMLR, 2022.
- Tsodyks, M. and Sejnowski, T. Associative memory and hippocampal place cells. *International Journal of Neural Systems*, 6:81–86, 1995.
- Veličković, P., Cucurull, G., Casanova, A., Romero, A., Liò, P., and Bengio, Y. Graph attention networks. In *International Conference on Learning Representations*, 2018. URL <https://openreview.net/forum?id=rJXMpikCZ>.
- Wang, Z. and Fan, J. Graph classification via reference distribution learning: Theory and practice. In *Advances in Neural Information Processing Systems*, 2024. URL <https://openreview.net/forum?id=1zVinhehks>.
- Wu, S., Wong, K. M., Fung, C. A., Mi, Y., and Zhang, W. Continuous attractor neural networks: candidate of a canonical model for neural information representation. *F1000Research*, 5:F1000–Faculty, 2016.
- Wu, W., Hsiao, T.-Y., Hu, J. Y.-C., Zhang, W., and Liu, H. In-context learning as conditioned associative memory retrieval. In *International Conference on Machine Learning*, 2025. URL <https://openreview.net/forum?id=Zup6F3MwQO>.
- Wu, Z., Pan, S., Chen, F., Long, G., Zhang, C., and Yu, P. S. A comprehensive survey on graph neural networks. *IEEE transactions on Neural Networks and Learning Systems*, 32(1):4–24, 2021.
- Yang, M., Shen, Y., Li, R., Qi, H., Zhang, Q., and Yin, B. A new perspective on the effects of spectrum in graph neural networks. In *International Conference on Machine Learning*, pp. 25261–25279. PMLR, 2022.
- Zhang, Z., Bu, J., Ester, M., Zhang, J., Li, Z., Yao, C., Dai, H., Yu, Z., and Wang, C. Hierarchical multi-view graph pooling with structure learning. *IEEE Transactions on Knowledge and Data Engineering*, 35(1):545–559, 2021.
- Zhao, Q. and Wang, Y. Learning metrics for persistence-based summaries and applications for graph classification. In *Advances in Neural Information Processing Systems*, pp. 9855–9866, 2019.
- Zhuge, M., Liu, H., Faccio, F., Ashley, D. R., Csordás, R., Gopalakrishnan, A., Hamdi, A., Hammoud, H. A. A. K., Herrmann, V., Irie, K., Kirsch, L., Li, B., Li, G., Liu, S., Mai, J., Piękos, P., Ramesh, A. A., Schlag, I., Shi, W., Stanić, A., Wang, W., Wang, Y., Xu, M., Fan, D.-P., Ghanem, B., and Schmidhuber, J. Mindstorms in natural language-based societies of mind. *Computational Visual Media*, 11(1):29–81, 2025. doi: 10.26599/CVM.2025.9450460.

## A. Notations Used in the Main Text and Appendices

Table 5 lists all the notations used in this paper.

Table 5. Notations used in this paper.

Notation	Description
$D$	Dimension of the state/token feature space
$N$	Number of tokens in the system
$\mathbf{x}$	Vector representation of token
$x_i$	Each element of $\mathbf{x}$
$X$	State matrix stacking token states, $X = [\mathbf{x}_1, \mathbf{x}_2, \dots, \mathbf{x}_N]^\top \in \mathbb{R}^{N \times D}$
$\mathbf{g}$	LayerNorm output applied to a token vector $\mathbf{x}$
$g_i$	Each element of $\mathbf{g}$
$G$	Normalized state matrix, $G = [\mathbf{g}_1, \dots, \mathbf{g}_N]^\top \in \mathbb{R}^{N \times D}$
$M$	Jacobian of LayerNorm, $M(\mathbf{x}(t)) = \nabla_{\mathbf{x}} \mathbf{g}(\mathbf{x}(t))$
$\mathcal{G}$	Relational structure (e.g., graph/topology) conditioning the dynamics/energy
$E(X; \mathcal{G})$	Total semantic energy of CDAT
$E^{\text{ATT-vMF}}$	Mo-vMF attention energy term
$E^{\text{HN}}$	Hopfield refinement energy term
$\lambda_v, \lambda_h$	Balancing weights for the Mo-vMF and Hopfield energy blocks
$\tau$	Time constant setting the scale of the dynamical system
$\Delta t$	Discrete time step size for Euler integration
$\alpha$	Euler step size, $\alpha := \Delta t / \tau$
$W$	Topology-conditioned coupling (mutual excitation) matrix, $W \in \mathbb{R}^{D \times D}$
$\omega$	Global damping/self-inhibition scalar decay rate
$V(t)$	Trajectory-wise storage functional (Lyapunov-type functional)
$J_0$	Excitation strength in the Gaussian coupling prior
$a$	Receptive range (bandwidth) in the Gaussian coupling prior
$W^{\text{train}}$	Learnable residual in the coupling, used in $W_{ij} = J_0 \exp(-d(i, j)^2 / 2a^2) + W_{ij}^{\text{train}}$
$d(i, j)$	Geodesic (structure-induced) distance between feature indices $i, j \in \{1, \dots, D\}$
$H$	Number of attention heads
$Y$	Dimension of the internal feature space for queries and keys
$Q, K$	Query/Key representations for attention (per head)
$P$	Number of local minima
$\beta$	Concentration parameter (inverse temperature) in the vMF distribution
$\mu_b, \pi_b$	Mean direction and mixture weight of component $b$ in Mo-vMF
$\xi_\mu$	Stored memory/prototype vector $\mu$ in the Hopfield module

## B. Experimental Details

### B.1. Dataset details

To comprehensively evaluate the effectiveness of CDAT, we conducted experiments on two distinct tasks: graph-level classification and graph anomaly detection. We utilized a total of ten standard benchmark datasets.

For the **Graph Classification** task, we selected 7 widely used benchmark datasets from the TUDataset collection (Morris et al., 2020). These include bioinformatics datasets (PROTEINS, NCI1, NCI109, DD, ENZYMES, MUTAG, MUTAGENICITY). These datasets vary significantly in terms of graph size, number of classes, and average node density.

For the **Graph Anomaly Detection** task, we employed three large-scale fraud detection datasets: YelpChi (Yelp), Amazon, and T-Finance. For the three datasets used in the experiments, Amazon and Yelp datasets can be obtained from the DGL library, while T-Finance can be obtained from (Tang et al., 2022). These datasets involve classifying nodes as either benign

or anomalous (fraudulent) based on their features and structural patterns.

The statistics of the datasets used in our experiments are summarized in Table 6 and Table 7.

Table 6. The statistics and properties of the seven datasets of TUDataset (additional node attributes are indicated by '+').

DATASET	GRAPHS	AVG. NODES	AVG. EDGES	NODE ATTR	CLASSES
MUTAG	188	17.93	19.79	7	2
ENZYMES	600	32.63	62.14	18 + 3	6
PROTEINS	1113	39.06	72.82	0 + 4	2
DD	1178	284.32	715.66	89	2
NCI1	4110	29.87	32.30	37	2
NCI109	4127	29.68	32.13	38	2
MUTAGENICITY	4337	30.32	30.77	14	2

Table 7. Summary of the graph anomaly detection datasets used in experiments.

DATASET	$ V $	$ E $	ANOMALY(%)	FEATURES
AMAZON	11944	4398392	6.87%	25
YELP	45954	3846979	14.53%	32
T-FINANCE	39357	21222543	4.58%	10

## B.2. Details of CDAT training on Anomaly Detection Task

We follow a unified training protocol across all datasets. Specifically, we train each model for 100 epochs using the Adam optimizer with a learning rate of 0.001, and report the average performance over 5 independent runs. Unless otherwise specified, we use a training ratio of 0.4, with the remaining nodes reserved for validation and testing.

For the model architecture, we keep most hyperparameters fixed (Table 8): we use 2 layers with 2 attention heads by default, enable LayerNorm while disabling BatchNorm, and adopt residual connections with dropout 0.1 and an FFN expansion ratio of 4. The default hidden dimension is 64. For the energy-iteration module, the default setting uses step size  $\alpha = 0.1$ , suppression coefficient 1.0, and noise standard deviation 0.02 (noise can be disabled by setting noise\_std=0).

We tune a small set of key hyperparameters on the validation set and select the best configuration within the 100-epoch budget for final test reporting. The tunable hyperparameters include hid\_dim, num\_heads, alpha, suppression\_coef, and noise\_std. The optimal per-dataset (and per-training-ratio) choices used in our experiments are summarized in Table 9. To speed up training, we enable subgraph sampling (subsample\_flag=1) and use a fixed subsampling ratio of 0.05 per epoch (sample\_ratio=0.05), which reduces computation while maintaining stable optimization.

## B.3. Details of CDAT training on Graph Classification Task

We train CDAT for 100 epochs with the Adam optimizer ( $b_1=0.9$ ,  $b_2=0.99$ ) using a peak learning rate of  $10^{-3}$ , a warmup period of 50 epochs, and a cosine-decay schedule to an initial/ending learning rate of  $5 \times 10^{-6}$ . We use a batch size of 64, weight decay 0.05, and do not apply gradient clipping. All experiments are conducted on a single GPU device. The full set of training and architecture hyperparameters is summarized in Table 10.

For the model architecture, we set the token/embedding dimension to 128 with 12 attention heads of head dimension 64. The softmax inverse temperature is initialized as  $\beta = 1/\sqrt{64}$  and is learned during training (train\_betas=Yes). CDAT uses an energy-iteration step size  $\alpha = 0.1$  with Gaussian noise of standard deviation  $\sigma_\varepsilon = 0.02$ . For graph spectral processing, we retain the top  $k = 15$  eigenvalues. The network depth is 1 with 4 blocks, using kernel size [3, 3] and dilation size [1, 1]. The Hopfield refinement module adopts a hidden dimension of 512 (i.e.,  $4 \times 128$ ), without bias in the Hopfield and attention modules, while LayerNorm keeps bias enabled. We fix the number of tokens to 500, use ReLU as the channel activation (chn\_atype=relu), and enable correlation computation (compute\_corr=True).

Table 8. Hyperparameter settings for node anomaly detection.

Training		
Parameter	Value	Note
dataset	amazon	—
train_ratio	0.4	—
epoch	100	—
run	5	—
seed	1	—
optimizer	Adam	—
lr	0.001	learning rate
sample_ratio	0.05	—
Architecture		
Parameter	Value	Note
hid_dim	64	hidden dimension
order	2	—
homo	1	—
n_layers	2	—
num_heads	2	—
layer_norm	True	—
batch_norm	False	—
residual	True	—
dropout	0.1	—
r	4	the dimension of matrix Q
ffn	4	FFN expansion ratio
Energy Iteration		
Parameter	Value	Note
alpha	0.1	energy iteration step size
suppression_coef	1.0	suppression coefficient
noise_std	0.02	base noise std; 0 disables noise
Other		
Parameter	Value	Note
num_class	2	—
subsample_flag	1	—
ablation_mode	False	—

### C. Ablation Study

Table 11 reports the ablation results on *graph-level classification*. We evaluate the two proposed dynamical components by disabling them individually. Removing *mutual excitation* leads to a clear performance drop on all datasets, with the most pronounced degradation on DD/NCI1/NCI109, indicating that structure-aware excitatory coupling is crucial for effective graph representation aggregation. In contrast, removing *self-inhibition* yields a smaller but still consistent decrease, suggesting that inhibitory control stabilizes the iterative dynamics and improves robustness across benchmarks. Combining both components (**CDAT Full**) achieves the best results, confirming that mutual excitation provides the primary gain while self-inhibition offers complementary stabilization and refinement.

In addition to the graph-level ablation in Table 11, we further conduct a more exhaustive study on anomaly detection by comparing **CDAT** variants against the strong baseline ET (Table 12). Specifically, we isolate the two key dynamical terms by keeping only the suppression/inhibition component (**SUPP**) or only the excitation-driven interaction component (**Wx**), and report MF1/AUC across different anomaly ratios in Table 12. Overall, neither isolated term alone consistently matches the full dynamics across datasets and ratios: **Wx** typically retains stronger discriminative ability, while **SUPP** can be less stable under harder settings (e.g., higher ratios), highlighting the necessity of combining excitation and inhibition (Table 12). Together with the ET comparison, these results provide a comprehensive validation that the gains of **CDAT** come from the proposed dynamical design rather than ad-hoc architectural changes (Table 12).

Table 9. Tunable hyperparameters used in each setting.

Dataset	Train ratio	hid_dim	num_heads	alpha	suppression_coef	noise_std
amazon	0.4	256	2	0.01	0.1	0
amazon	0.01	256	2	0.01	0.5	0
amazon	0.7	256	4	0.1	0.1	0
tfinance	0.7	128	4	0.01	0.1	0
tfinance	0.4	128	4	0.01	0.5	0
tfinance	0.01	128	4	0.01	1.0	0.02
yelp	0.4	128	4	0.01	0.1	0
yelp	0.7	256	2	0.05	0.1	0.02
yelp	0.01	256	4	0.01	1.0	0

Table 10. Hyperparameter and architecture choices for CDAT during TUDataset experiments.

Training		Architecture	
Parameter	Value	Parameter	Value
batch_size	64	token_dim	128
epochs	100	num_heads	12
peak lr	$10^{-3}$	head_dim	64
warmup_epochs	50	$\beta$	$1/\sqrt{64}$
initial and ending lr	$5 \times 10^{-6}$	train_betas	Yes
$b_1, b_2$ (Adam)	0.9, 0.99	step size $\alpha$	0.1
weight_decay	0.05	$k$ eigenvalues	15
grad_clipping	None	noise $\sigma_{noise}$	0.02
num. of gpu devices	1	depth	1
r	4	block	4
—	—	kernel_size	[3, 3]
—	—	dilation_size	[1, 1]
—	—	hidden_dim (HN)	512
—	—	bias in HN	None
—	—	bias in ATT-vMF	None
—	—	bias in LNORM	Yes
—	—	num_tokens	500
—	—	chn_atype	relu
—	—	compute_corr	True
—	—	avg. total #params	1,066,855

## D. Parameter Comparison

Tables 13 and 14 compare the parameter counts of our full model **CDAT** and the **ET** ablation. On the anomaly detection setting (Tables 13), CDAT and ET have identical parameters per Transformer block, while CDAT has a slightly larger total parameter count. This is expected: our improvement is not introduced by modifying the internal architecture of each block, but by adding extra dynamical control terms (state-dependent modulation variables) outside the standard block parameterization. Therefore, the additional parameters appear only in the global model budget, leaving the per-block parameter count unchanged. On graph classification (Tables 14), we observe a similarly small gap between CDAT and ET, indicating that the proposed dynamics incurs only a negligible parameter overhead overall.

## E. Additional Proofs

### E.1. Proof of Theorem 3.1

*Proof.* Consider the continuous-time dynamics of a single token state  $\mathbf{x}(t) \in \mathbb{R}^D$ . In the context of Continuous Attractor Neural Networks (CANNs), the indices  $i \in \{1, \dots, D\}$  do not represent independent semantic features, but rather discrete coordinates on a latent topological manifold (e.g., a grid or a graph).

The mutual excitation component of the dynamics is given by  $\tau \dot{\mathbf{x}} = W\mathbf{x}$ . Applying a first-order Euler discretization with

Table 11. Ablation study on graph classification benchmarks. Accuracy (%) is reported.

Setting (ablation)	DD	NCI1	NCI109	MUTAG
Mutual Excitation	83.09	82.84	84.89	96.27
Self-Inhibition	98.09	92.74	92.07	98.46
<b>CDAT(Full)</b>	<b>98.50</b>	<b>93.50</b>	<b>94.30</b>	<b>98.80</b>

Table 12. Comprehensive ablation on anomaly detection across different anomaly ratios. We report MF1 and AUC (% , mean  $\pm$  std). ET is the baseline; **SUPP** and **Wx** are term-wise variants; **CDAT (Full)** corresponds to the complete model.

Dataset	Ratio	ET	SUPP	Wx	CDAT (Full)
<b>MF1 (%)</b>					
amazon	0.01	89.42 $\pm$ 5.80	90.04 $\pm$ 1.60	89.42 $\pm$ 5.80	91.2 $\pm$ 0.9
amazon	0.40	90.39 $\pm$ 1.02	91.39 $\pm$ 1.59	89.90 $\pm$ 1.67	92.1 $\pm$ 0.6
amazon	0.70	92.05 $\pm$ 3.58	85.82 $\pm$ 10.81	90.99 $\pm$ 3.83	91.9 $\pm$ 0.1
tfinance	0.01	86.09 $\pm$ 1.42	59.53 $\pm$ 6.49	85.66 $\pm$ 1.21	87.4 $\pm$ 1.1
tfinance	0.40	91.49 $\pm$ 2.16	86.42 $\pm$ 2.50	91.49 $\pm$ 2.16	90.6 $\pm$ 0.6
yelp	0.01	62.74 $\pm$ 1.93	61.99 $\pm$ 0.73	61.94 $\pm$ 0.88	63.0 $\pm$ 1.4
yelp	0.40	69.52 $\pm$ 0.22	68.74 $\pm$ 2.05	69.91 $\pm$ 1.34	70.5 $\pm$ 0.1
yelp	0.70	70.30 $\pm$ 3.69	64.57 $\pm$ 1.32	69.21 $\pm$ 0.96	71.5 $\pm$ 0.2
<b>AUC (%)</b>					
amazon	0.01	94.51 $\pm$ 1.19	95.43 $\pm$ 1.78	94.51 $\pm$ 1.14	94.5 $\pm$ 1.1
amazon	0.40	95.72 $\pm$ 2.02	95.10 $\pm$ 1.23	96.04 $\pm$ 2.29	97.2 $\pm$ 0.2
amazon	0.70	97.07 $\pm$ 4.15	92.90 $\pm$ 5.03	97.07 $\pm$ 4.15	93.0 $\pm$ 5.0
tfinance	0.01	92.25 $\pm$ 1.11	79.04 $\pm$ 3.08	92.68 $\pm$ 1.72	95.9 $\pm$ 0.4
tfinance	0.40	96.72 $\pm$ 1.70	93.65 $\pm$ 1.02	97.23 $\pm$ 1.98	97.8 $\pm$ 1.1
yelp	0.01	72.86 $\pm$ 1.26	73.05 $\pm$ 1.43	73.30 $\pm$ 1.59	74.3 $\pm$ 0.3
yelp	0.40	83.57 $\pm$ 2.75	81.70 $\pm$ 2.08	83.45 $\pm$ 2.69	84.4 $\pm$ 0.2
yelp	0.70	81.65 $\pm$ 0.96	78.24 $\pm$ 4.52	82.22 $\pm$ 0.32	91.9 $\pm$ 0.3

step size  $\Delta t$  and  $\alpha := \Delta t/\tau$ , we obtain the update rule for the  $i$ -th neuron:

$$x_i^{(t+1)} = x_i^{(t)} + \alpha \sum_{j=1}^D W_{ij} x_j^{(t)}. \quad (16)$$

In our formulation, the coupling matrix  $W \in \mathbb{R}^{D \times D}$  is parameterized as a kernelized prior plus a learnable residual:

$$W_{ij} = J_0 \exp\left(-\frac{d(i, j)^2}{2a^2}\right) + W_{ij}^{train}, \quad (17)$$

where  $d(i, j)$  is the geodesic distance between neuron  $i$  and neuron  $j$  on the feature manifold.

Let  $\mathcal{K}_{ij} = J_0 \exp(-d(i, j)^2/2a^2)$ . The term  $\sum_j \mathcal{K}_{ij} x_j$  represents a discrete approximation of the continuous convolution of the signal  $x$  with a Gaussian kernel:

$$(x * \mathcal{K})(i) \approx \sum_{j=1}^D \mathcal{K}_{ij} x_j. \quad (18)$$

In Graph Signal Processing (GSP), this operation is precisely a **spatial graph convolution** (or heat diffusion) on the graph defined by the neurons, with  $\mathcal{K}$  acting as the diffusion filter.

Furthermore, we can define an effective adjacency matrix  $\tilde{A}$  for this latent graph where  $\tilde{A}_{ij} = \alpha W_{ij}$ . The update rule then becomes:

$$\mathbf{x}^{(t+1)} = \mathbf{x}^{(t)} + \tilde{A}\mathbf{x}^{(t)} = (I + \tilde{A})\mathbf{x}^{(t)}. \quad (19)$$

This form is algebraically equivalent to a layer of a **Residual Graph Convolutional Network (ResGCN)** operating on the *feature graph* (where nodes are feature dimensions), rather than the input data graph.

Table 13. Comparison between the number of parameters in our full model **CDAT** and the **ET** on anomaly detection task.

Model	NParams		NParams (per block)	
CDAT	4.29M	↓0.00%	0.59M	↓0.00%
ET	4.25M	↓1.11%	0.59M	↓0.00%

Table 14. Parameter comparison between **CDAT** and **ET** on graph classification task.

Model	NParams	
CDAT	1.060M	↓0.00%
ET	1.058M	↓0.19%

Thus, the mutual excitation term strictly enforces a topological prior: it diffuses activity among neighboring neurons in the latent space, smoothing the representation locally according to the manifold structure defined by  $d(i, j)$ , while the learnable term  $W^{train}$  allows for non-local "shortcut" connections similar to long-range dependencies in modern GCNs. This proves that the update step is a residual convolution on the feature manifold.  $\square$

### E.2. Proof of Theorem 3.3

*Proof.* Let  $\mathbf{x}(\cdot)$  be any  $C^1$  solution of the dynamics and define  $\mathbf{g}(t) := \mathbf{g}(\mathbf{x}(t))$ . Assume  $E, \mathbf{g} \in C^1$  and  $W = W^\top$ . Fix  $t_0$  and define the trajectory-wise storage functional

$$V(t) := E(\mathbf{g}(t)) + \int_{t_0}^t \left( (1 + \omega)\mathbf{x}(s) - W\mathbf{x}(s) \right)^\top \dot{\mathbf{g}}(s) ds, \quad (20)$$

where  $\dot{\mathbf{g}}(s) = \frac{d}{ds}\mathbf{g}(\mathbf{x}(s))$ . Since  $\mathbf{x}(\cdot)$  is  $C^1$  and  $\mathbf{g} \in C^1$ , the integrand is continuous, hence the integral is well-defined.

By the chain rule,

$$\frac{d}{dt}E(\mathbf{g}(t)) = \nabla_{\mathbf{g}}E(\mathbf{g}(t))^\top \dot{\mathbf{g}}(t). \quad (21)$$

Applying Leibniz' rule to the time integral in (20) yields

$$\frac{d}{dt} \int_{t_0}^t \left( (1 + \omega)\mathbf{x}(s) - W\mathbf{x}(s) \right)^\top \dot{\mathbf{g}}(s) ds = \left( (1 + \omega)\mathbf{x}(t) - W\mathbf{x}(t) \right)^\top \dot{\mathbf{g}}(t). \quad (22)$$

Combining (21) and (22), we obtain

$$\dot{V}(t) = \left( \nabla_{\mathbf{g}}E(\mathbf{g}(t)) + (1 + \omega)\mathbf{x}(t) - W\mathbf{x}(t) \right)^\top \dot{\mathbf{g}}(t). \quad (23)$$

Rearranging the dynamics gives

$$\nabla_{\mathbf{g}}E(\mathbf{g}(t)) + (1 + \omega)\mathbf{x}(t) - W\mathbf{x}(t) = -\tau \dot{\mathbf{x}}(t). \quad (24)$$

Substituting (24) into (23) yields

$$\dot{V}(t) = -\tau \dot{\mathbf{x}}(t)^\top \dot{\mathbf{g}}(t). \quad (25)$$

Let  $M(\mathbf{x}) := \nabla_{\mathbf{x}}\mathbf{g}(\mathbf{x})$ . Therefore,

$$\dot{V}(t) = -\tau \dot{\mathbf{x}}(t)^\top M(\mathbf{x}) \dot{\mathbf{x}}(t). \quad (26)$$

If  $M(\mathbf{x}(t)) \succeq 0$  (e.g., by Lemma 3.2 for LayerNorm with  $\gamma > 0$ ), then  $\dot{V}(t) \leq 0$ , hence  $V(t)$  is non-increasing.  $\square$

### E.3. Proof of Theorem 4.1

*Proof.* By the Boltzmann principle, the probability of a configuration indexed by  $l$  is proportional to the exponential of minus its energy,

$$p_l \propto \exp(-\beta E_l). \quad (27)$$

Now consider a mixture of von Mises–Fisher distributions on  $S^{Y-1}$  with density

$$p(x) = \sum_{B=1}^N \pi_B C_Y(\kappa) \exp(\kappa \mu_B^\top x), \quad (28)$$

where all components share the same concentration parameter  $\kappa > 0$ , the mean directions satisfy  $\|\mu_B\| = 1$ , and  $C_Y(\kappa)$  denotes the normalization constant. Moreover, the mask  $B \neq C$  in (14) corresponds to a query-dependent mixture that excludes the  $B = C$  component, *i.e.*,

$$\pi_{B|C} = \begin{cases} \frac{1}{N-1}, & B \neq C, \\ 0, & B = C. \end{cases}$$

To match the attention log-sum-exp over keys for each query, we identify

$$\kappa = \beta, \quad x = K_C, \quad \mu_B = Q_B.$$

Under this identification, the negative log-marginal likelihood of observing  $K_C$  becomes

$$\begin{aligned} -\log p(K_C) &= -\log \left( \sum_{B \neq C} \frac{1}{N-1} C_Y(\beta) \exp(\beta Q_B^\top K_C) \right) \\ &= -\log \left( \sum_{B \neq C} \exp(\beta Q_B^\top K_C) \right) + \text{const}, \end{aligned} \quad (29)$$

where the constant absorbs  $\log C_Y(\beta)$  and  $\log N$ .

Comparing (29) with the per-token contribution in (14), we observe that the self-attention energy associated with each key  $K_C$  is proportional to the negative log-likelihood under the Mo–vMF model. According to the Boltzmann principle, we know

$$E^{K_C} \propto -\log p(K_C). \quad (30)$$

Aggregating over all keys yields the global energy

$$E^{\text{global}} = \sum_{C=1}^N E^{K_C} \propto -\frac{1}{\beta} \sum_{C=1}^N \log \left( \sum_{B \neq C} \exp(\beta Q_B^\top K_C) \right), \quad (31)$$

which matches the self-attention energy (11) up to global constants. □

## F. Algorithm

---

**Algorithm 1** Training and inference pseudocode of CDAT
 

---

```

1: HyperParameters
2: rollout steps  $T$ ; step size  $\Delta t$ ; time constant  $\tau$  (thus  $\alpha = \Delta t/\tau$ ); epochs  $N_{\text{epoch}}$ ; batch size  $B$ ; inverse temperature  $\beta$ ;
   learning rate  $\eta$ 
3: Parameters
4: feature coupling  $W \in \mathbb{R}^{D \times D}$ 
5: attention kernels  $W^Q, W^K \in \mathbb{R}^{Y \times H \times D}$ ; Hopfield memory  $\xi \in \mathbb{R}^{P \times D}$ 
6: decay rate  $\omega \in \mathbb{R}_{>0}$ ; LayerNorm params  $(\gamma_{\text{norm}}, \delta_{\text{norm}})$ ; balancing weights  $\lambda_v, \lambda_h$ 
7: decoder parameters  $\Psi$ 
8: dynamics parameters  $\Theta$ 

10: Infer // state dynamics rollout
11: Inputs: corrupted/initial tokens  $X_0 \in \mathbb{R}^{N \times D}$ 
12: Initialize  $X \leftarrow X_0, \alpha \leftarrow \Delta t/\tau$ 
13: for  $t = 0$  to  $T - 1$  do
14:    $G \leftarrow \text{LayerNorm}(X; \gamma_{\text{norm}}, \delta_{\text{norm}})$ 
15:    $Q \leftarrow G(W^Q)^\top, K \leftarrow G(W^K)^\top$ 
16:    $E^{\text{HN}} \leftarrow -\sum_{b=1}^N \sum_{\mu=1}^P \text{ReLU}\left(\sum_{j=1}^D \xi_{\mu j} G_{bj}\right)$ 
17:    $E^{\text{ATT-vMF}} \leftarrow -\frac{1}{\beta} \sum_{c=1}^N \log\left(\sum_{b \neq c} \exp(\beta Q_b^\top K_c)\right)$ 
18:    $E \leftarrow \lambda_v E^{\text{ATT-vMF}} + \lambda_h E^{\text{HN}}$ 
19:    $U \leftarrow \nabla_G E$ 
20:    $F_{\text{exc}} \leftarrow WX$ 
21:    $F_{\text{dec}} \leftarrow -(1 + \omega)X$ 
22:    $X \leftarrow X + \alpha(F_{\text{exc}} + F_{\text{dec}} - U)$ 
23: end for
24: Output: refined tokens  $X_T \leftarrow X$ 

26: Train
27: Inputs: training set  $\mathcal{S} = \{(X_0^{(n)}, y^{(n)})\}$  //  $X$  is the clean target tokens
28: for epoch = 1 to  $N_{\text{epoch}}$  do
29:   for each mini-batch  $\mathcal{B} \subset \mathcal{S}$  do
30:      $\mathcal{L}_{\mathcal{B}} \leftarrow 0$ 
31:     for each  $(X_0, y) \in \mathcal{B}$  do
32:        $X_T \leftarrow \text{INFER}(X_0)$ 
33:        $\hat{y} \leftarrow \text{Dec}_{\Psi}(X_T)$  // decode refined tokens
34:        $\mathcal{L}_{\mathcal{B}} \leftarrow \mathcal{L}_{\mathcal{B}} + \text{MSE}(\hat{y}, y)$ 
35:     end for
36:      $\mathcal{L}_{\mathcal{B}} \leftarrow \mathcal{L}_{\mathcal{B}}/|\mathcal{B}|$ 
37:      $\Theta \leftarrow \Theta - \eta \nabla_{\Theta} \mathcal{L}_{\mathcal{B}}, \Psi \leftarrow \Psi - \eta \nabla_{\Psi} \mathcal{L}_{\mathcal{B}}$ 
38:   end for
39: end for
40: Return trained parameters  $(\Theta, \Psi)$ 

```

---